

Large-Scale Errors and Mesoscale Predictability in Pacific Northwest Snowstorms

DALE R. DURRAN

Department of Atmospheric Sciences, University of Washington, Seattle, Washington

PATRICK A. REINECKE AND JAMES D. DOYLE

Naval Research Laboratory, Monterey, California

(Manuscript received 16 July 2012, in final form 20 November 2012)

ABSTRACT

The predictability of lowland snow in the Puget Sound region of the Pacific Northwest is explored by analyzing the spread in 100-member ensemble simulations for two events from December 2008. Sensitivities to the microphysical and boundary layer parameterizations in these simulations are minimized by estimating the likely precipitation type from the forecast 850-hPa temperatures and the established rain–snow climatology. Results suggest that the ensemble spread in events such as these, which were triggered by amplifying short waves, may develop a significant fraction of both rain-likely members and snow-likely members at forecast lead times as short as 36 h.

The perturbation kinetic energy of the ensemble members about the ensemble mean ($\overline{KE'}$) is not maximized at small scales. Instead, the power in the initial spectrum of $\overline{KE'}$ produced by the authors' ensemble Kalman filter (EnKF) data assimilation cycle increases with increasing horizontal scale. The power in $\overline{KE'}$ subsequently grows with time, while maintaining approximately the same spectral shape. There is no evidence of small-scale perturbations developing rapidly and transferring their influence upscale. Instead, the large-scale perturbations appear to grow more rapidly during the first 12 h than those at the smallest resolved scales.

1. Introduction

The development of mesoscale numerical weather prediction (NWP) models over the last two decades has made deterministic forecasts using horizontal grid spacings of about 5 km available to the operational and research communities. Nevertheless, the predictability of the mesoscale features captured in such forecasts remains unclear. Early investigations of predictability (Lorenz 1969) suggested that atmospheric circulations with characteristic scales of 20–40 km would have very limited predictability. Later researchers arrived at much more optimistic estimates, noting that many mesoscale phenomena are produced (i) by interactions between known small-scale forcing agents, like topography or land–sea contrasts, and the relatively predictable large-scale flow, or (ii) by the large-scale features themselves through processes such as frontogenesis (Anthes et al. 1985).

Subsequent research has shown that some of the sources of enhanced mesoscale predictability identified by Anthes et al. (1985) arose through nonphysical sources such as a lack of variability in the forcing at lateral boundaries (Vukicevic and Errico 1990; Laprise et al. 2000). In addition, it is widely recognized that atmospheric processes generated through instabilities acting at very small scales, such as deep convection, are not likely to be predictable over periods dramatically longer than those suggested by their short eddy turnover times (Hohenegger and Schär 2007). Nevertheless, the idea that many mesoscale phenomena can inherit extended predictability from the synoptic-scale flow remains a dominant paradigm in mesoscale meteorology. For example, Mass et al. (2002) note that in the Pacific Northwest, “most of the region’s mesoscale circulations are created by the interaction of the synoptic-scale flow with the mesoscale terrain; thus, mesoscale predictability is substantially controlled by longer-lived synoptic predictability” (p. 424).

In this study we revisit the question of whether mesoscale features forced by the larger-scale flow enjoy enhanced predictability relative to what might be

Corresponding author address: Dale R. Durran, Box 351640, Dept. of Atmospheric Sciences, University of Washington, Seattle, WA 98125.
E-mail: durrand@atmos.washington.edu

expected based on turbulence models. Toward this end we will examine the sensitivity of the rain–snow boundary in developing cyclones to small variations in the initial and boundary conditions among 100-member ensemble simulations. Variations in the location of the rain–snow boundary occur over mesoscale dimensions of 10–100 km, and the location of this boundary might be expected to inherit much of the predictability associated with the larger-scale flow. In particular, we simulate two events that brought a threat of lowland snow to the Pacific Northwest in December 2008 using the Coupled Ocean–Atmosphere Mesoscale Prediction System (COAMPS; Hodur 1997). In analyzing these ensembles, our first goal is to determine the time interval over which the ensemble spread becomes large enough to include both many members likely to produce rain and many likely to produce snow. This provides an estimate of the forecast interval beyond which initial-condition uncertainty might be expected to significantly limit the reliability of single deterministic forecasts of these events. Our second goal will be to examine the evolution of the perturbation kinetic energy of the ensemble members about the ensemble mean to see how closely this evolution follows the classical paradigm in which small-scale initial differences progressively spread to larger scales.

2. Experimental design

While December 2008 was a particularly snowy month for the Pacific Northwest [35.3 in. (89.7 cm) fell at the Seattle–Tacoma (Sea–Tac) International Airport compared to a climatological value of 6.4 in. (16.3 cm)], considerable forecast uncertainty was present in the day-to-day weather discussions generated by the Seattle National Weather Service Office. We focus on two events from this month that brought a threat of snow to the Puget Sound lowlands of western Washington.

a. Determination of precipitation type

The type of precipitation falling at the surface is sensitively dependent on microphysical processes and the vertical profile of temperature near the surface (Thériault et al. 2010). In all numerical weather prediction models, these variables are largely controlled by cloud microphysical and boundary layer parameterizations, both of which can introduce significant error. In this study we attempt to sidestep the errors that might be generated by these parameterizations by focusing on the behavior of features that can be more confidently simulated by the model: the 850-hPa temperature and the presence of any type of precipitation.

Ferber et al. (1993, hereafter FMLP) showed that likely-rain and likely-snow events at Sea–Tac airport in

the Puget Sound lowlands can be distinguished by the 850-hPa temperature. In particular, they investigated the climatological characteristics of the wintertime precipitation at Sea–Tac and found a transition from almost completely rain to almost completely snow as 850-hPa temperatures ranged between -4° and -8°C . We will therefore assess initial-condition sensitivity by examining the ensemble spread in the 850-hPa temperature during periods of precipitation. As a consequence, our results should be relatively independent of the details of the boundary layer and microphysical parameterizations.

The FMLP climatology was based on radiosonde data from Quillayute on the Olympic Peninsula. Clearly the temperature directly above the region of interest is likely to have a more immediate physical connection to the processes determining the type of precipitation, so we define the 850-hPa temperature metric as the average over the rectangle shown in Fig. 1b. The precise 850-hPa temperatures over which the rain–snow transition occurs may be slightly different in the metric box from those over Quillayute and may also correspond to different forecast temperatures owing to biases in the model, but we will nevertheless assume the transition from likely-rain to likely-snow events occurs over an 850-hPa metric box temperature range of about 4°C .

b. Numerical model

The atmospheric module of the COAMPS model is used in this study. This model is based on a finite-difference approximation to the fully compressible, non-hydrostatic equations and uses a terrain-following vertical coordinate transformation. The compressible equations are integrated using a time-splitting technique with a semi-implicit formulation for the vertical acoustic modes (Klemp and Wilhelmson 1978). Horizontal advection is computed using fourth-order spatial differencing.

A prognostic equation for the turbulence kinetic energy (TKE) budget is used to represent the planetary boundary layer and free-atmospheric turbulent mixing and diffusion (Hodur 1997). The Louis (1979) surface-layer parameterization, which makes use of a surface energy budget based on the force–restore method, is used to represent the surface fluxes. Subgrid-scale moist convection is represented using the Kain and Fritsch (1993) parameterization. The grid-scale evolution of the moist processes is predicted explicitly from budget equations for cloud water, cloud ice, raindrops, snowflakes, and water vapor (Rutledge and Hobbs 1983). The short- and longwave radiation processes are represented following Harshvardhan et al. (1987). Lateral boundary conditions for the outermost grid mesh are based on forecast fields from the Navy Operational Global Analysis and Prediction System (NOGAPS). Results

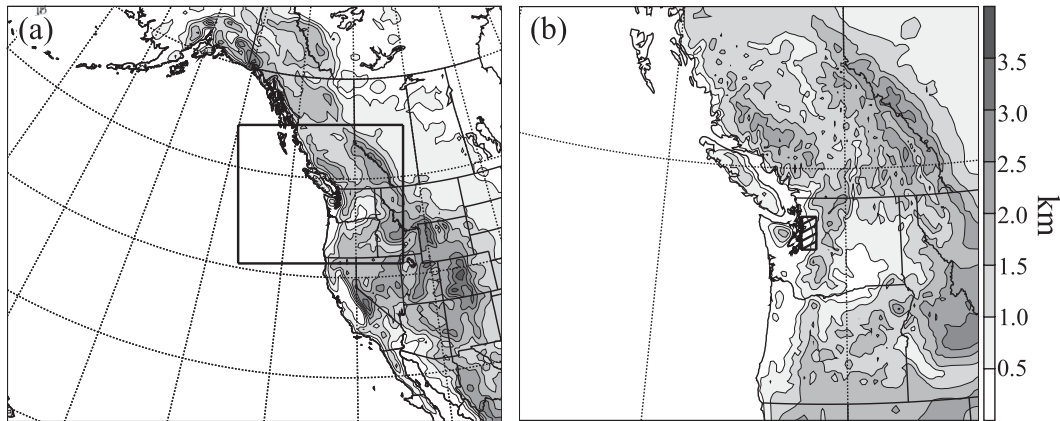


FIG. 1. The topography and location of the (a) 36- and (b) 12-km domains. The location of the 12-km domain is indicated by the solid line in (a). The location of the Puget Sound metric box is indicated by the hashed box in (b).

from COAMPS model simulations have been evaluated on numerous occasions using special observations and field campaign datasets and have been demonstrated to accurately simulate mesoscale flows influenced by topography (e.g., Doyle et al. 2011, 2009; Jiang and Doyle 2009; Reinecke and Durran 2009b).

The COAMPS forecasts were performed using two horizontally nested grid meshes, each with 151×127 grid points with horizontal grid increments on the computational meshes of 36 and 12 km (see Figs. 1a and 1b, respectively). The COAMPS model contains 40 vertical levels on a nonuniform vertical grid consisting of an increment of 10 m at the lowest level that gradually increases up to the model top at 30 km. The grid meshes are one-way interactive. A sponge upper-boundary condition is applied to mitigate the reflection of vertically propagating gravity waves over the top 10 km of the model. The topographic data are based on the U.S. Defense Mapping Agency (DMA) 100-m-resolution dataset.

c. Ensemble methodology

1) ENSEMBLE GENERATION

To generate the 100-member ensemble, a cycling data assimilation system utilizing a square-root version of the ensemble Kalman filter (EnKF; Whitaker and Hamill 2002) was established. The initial ensemble perturbations were created by drawing random fields of horizontal wind, potential temperature, and water vapor from the Weather Research and Forecasting (WRF) model-based variational data assimilation system (WRF-Var) static covariance model (Barker et al. 2004). The standard deviation of these perturbations was scaled by a factor of 1.25 and added to a 24-h NOGAPS forecast valid at 1200 UTC 5 December 2008, which was then interpolated to the 36- and 12-km COAMPS domains.

Prior to data assimilation, the initial perturbations were allowed to adjust to the COAMPS attractor by integrating the ensemble for 24 h.

2) DATA ASSIMILATION ENSEMBLE

The EnKF data assimilation ensemble was cycled every 6 h from 1200 UTC 6 December to 1200 UTC 18 December 2008. Observations from radiosonde ascents, Automated Surface Observing Systems (ASOS) data, Aircraft Communications Addressing and Reporting System (ACARS) data, and satellite-derived atmospheric motion vectors were assimilated every 6 h with the EnKF. The assimilation was performed independently on the 36- and 12-km grids, which is consistent with the one-way nesting strategy described above. To prevent spurious long-distance correlations from contaminating the data assimilation, a standard Gaspari-Cohn (Gaspari and Cohn 1999) localization with radii of 3000 and 1500 km are applied to the covariance for the respective 36- and 12-km domains. Furthermore, the Zhang et al. (2004) covariance blending inflation method is used with $\alpha = 0.25$ for the 36-km domain and $\alpha = 0.5$ for the 12-km domain. Lateral boundary conditions are perturbed via the fixed covariance perturbation method described in Torn et al. (2006) using perturbations drawn from the WRF-Var static covariance model (Barker et al. 2004). The perturbations were applied to the lateral boundaries every 6 h with an autocorrelation of 0.75 and a scaling factor of 1.75 (Torn et al. 2006; Torn and Hakim 2008). Innovation statistics from the 12-day experiment were used to verify that the prior ensemble spread was well calibrated to the ensemble-mean error at forecast hour 6 (not shown). Limitations on our computational resources prevented us from performing enough 36-h forecasts to assess the ensemble calibration at longer lead times.

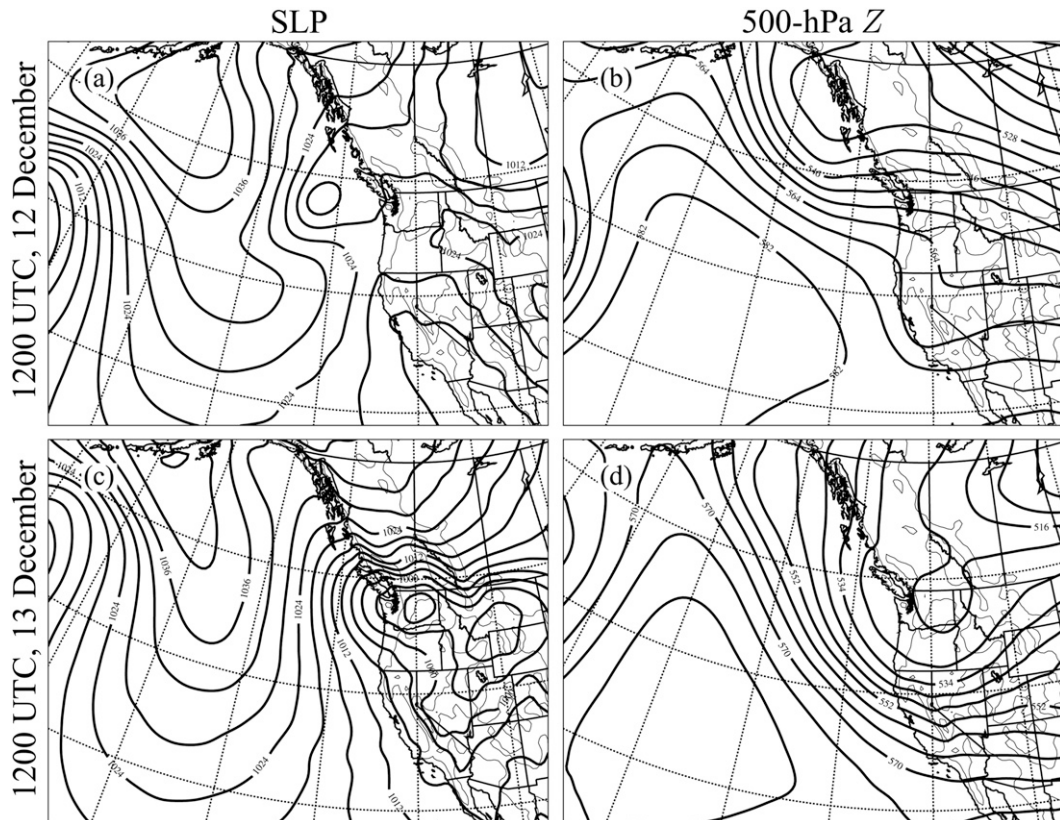


FIG. 2. The 100-member ensemble-mean analysis for the 12–13 December event. Plotted are the analyzed (a) sea level pressure and (b) 500-hPa geopotential heights at 1200 UTC 12 Dec 2008 and the (c) sea level pressure and (d) 500-hPa geopotential heights at 1200 UTC 13 Dec 2008.

3) FORECAST ENSEMBLE

From the data assimilation procedure described above, a 100-member forecast ensemble was generated by directly applying the EnKF analysis perturbations to the ensemble-mean analysis. Two sets of ensemble forecasts were performed to examine the 24–36-h growth of perturbations initialized at 1200 UTC 13 December and 1200 UTC 18 December 2008. To this end 36-h ensemble forecasts are initialized every 12 h from 0000 UTC 12 December to 0000 UTC 13 December and from 0000 UTC 17 December to 0000 UTC 18 December. The lateral boundary perturbations for the forecast ensemble were constructed in a similar manner as those for the data assimilation ensemble. The impact of introducing perturbations at the lateral boundaries is investigated below.

d. Synoptic-scale overview

The ensemble-mean COAMPS EnKF analyses for sea level pressure and the 500-hPa height fields are shown for 1200 UTC on 12 and 13 December 2008 in Fig. 2. Reminiscent of the FMLP composite analysis for snow at

Sea–Tac, 24 h prior to the event a broad 500-hPa westerly flow is impinging upon western Washington and southwestern British Columbia, and a short-wave trough (between 140° and 130°W in Fig. 2b) is embedded in northwest flow farther upstream. As shown in Fig. 2a, a surface cyclone associated with the 500-hPa short-wave trough is present just west of Vancouver Island. Twenty-four hours later, at 1200 UTC 13 December, the 500-hPa trough has progressed eastward and deepened with the trough axis extending from central Washington southward toward Southern California (Fig. 2d). Likewise, the surface cyclone has also progressed eastward across the Puget Sound and is now located over eastern Washington (Fig. 2c).

Figure 3 shows the ensemble-mean COAMPS EnKF analyses of sea level pressure and 500-hPa geopotential heights for 1200 UTC 17 December and 1200 UTC 18 December 2008. The general structure of the synoptic flow is similar to that in the 12–13 December case, although the positions of the short wave and surface low 24 h prior to the event are farther east (Figs. 3a,b). In both cases, variations in the evolution of the surface cyclone appear to be the primary source of ensemble spread in the snow forecasts.

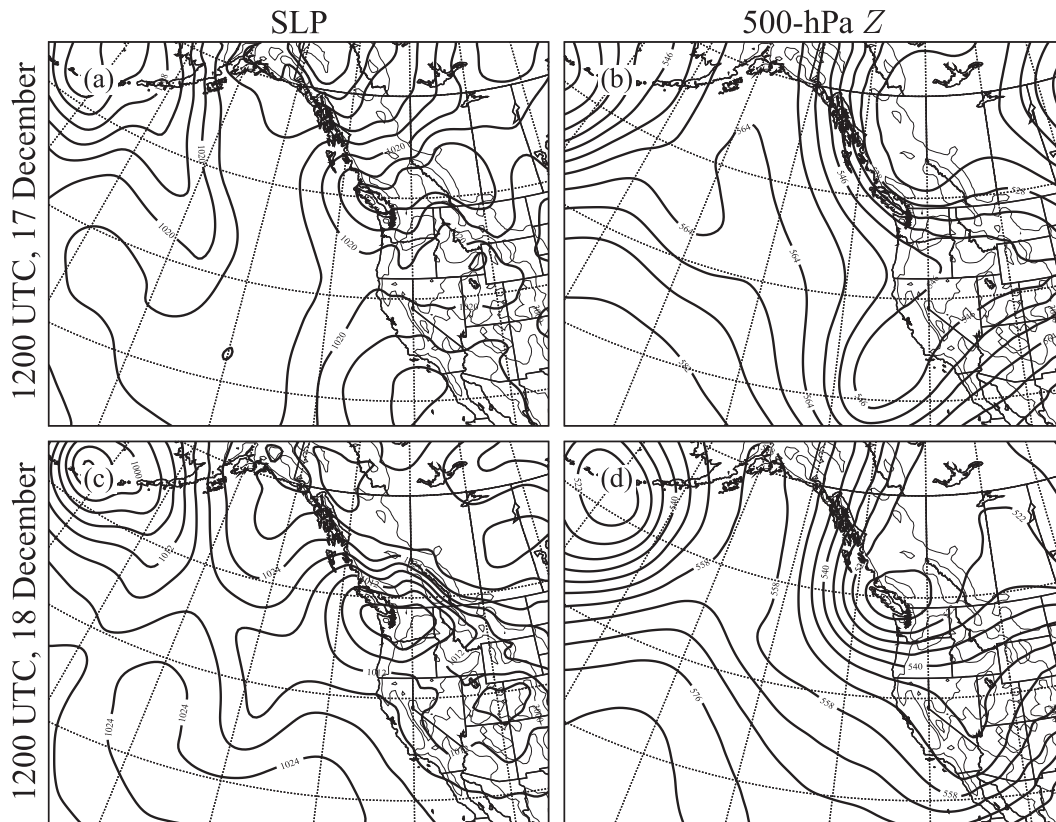


FIG. 3. As in Fig. 2, but for (a),(b) 1200 UTC 17 Dec and (c),(d) 1200 UTC 18 Dec 2008.

3. Ensemble spread in the 850-mb temperature forecasts

a. The 12–13 December case

The spread of the 850-hPa temperature metric in the 12–13 December case is shown as a function of forecast lead time by the box-and-whisker plots in Fig. 4a. In these plots, the box portion represents the range of temperatures contained within one standard deviation σ of the ensemble mean at the verification time of 1200 UTC 13 December 2008. The whiskers attached to each box show the range of temperatures falling outside of the 1σ envelope. Thus, for our 100-member ensemble the upper whisker indicates the range of the 17 warmest ensemble members while the lower whisker spans the range of the 17 members with the coldest temperatures in the metric box. The mean of the full ensemble is plotted as a horizontal line inside each box, and the means of the subsets of the 17 warmest and coldest members are shown by the dots on each whisker.

The ensemble-mean temperature in Fig. 4a is between -5° and -5.5°C at all forecast lead times (and drops to about -6.5°C in the verifying analysis). The forecast spread increases with increasing lead times, and the

difference between the means of the warm and cold subsets increases most rapidly between the forecast lead times of 24 and 36 h. The mean of the 17 warm-subset members for the 36-h forecast is -2.5°C , so according to the FMLP climatology, any precipitation associated with these warm-subset members should fall as rain. On the other hand, the mean temperature for the cold subset at the 36-h lead time is -8°C , and the FMLP climatology suggests any precipitation would fall as snow. A variety of more borderline cases are contained within the other 66 members of the ensemble, but it is noteworthy that the ensemble spread is sufficient to include a significant number of both likely-rain and likely-snow cases with 5.5°C separating the temperatures of the warm- and the cold-subset means.¹

The evolution of the 850-mb temperature metric during the 36-h forecasts is plotted as a function of

¹ As noted previously, the spread in the 850-hPa metric box temperature likely has more significance for predictability than do the specific temperature values for a particular snow forecast, since the FMLP climatology is based on the temperature of the Quilayute sounding (which lies outside the metric box) and the COAMPS 850-hPa temperatures are not corrected for model bias.

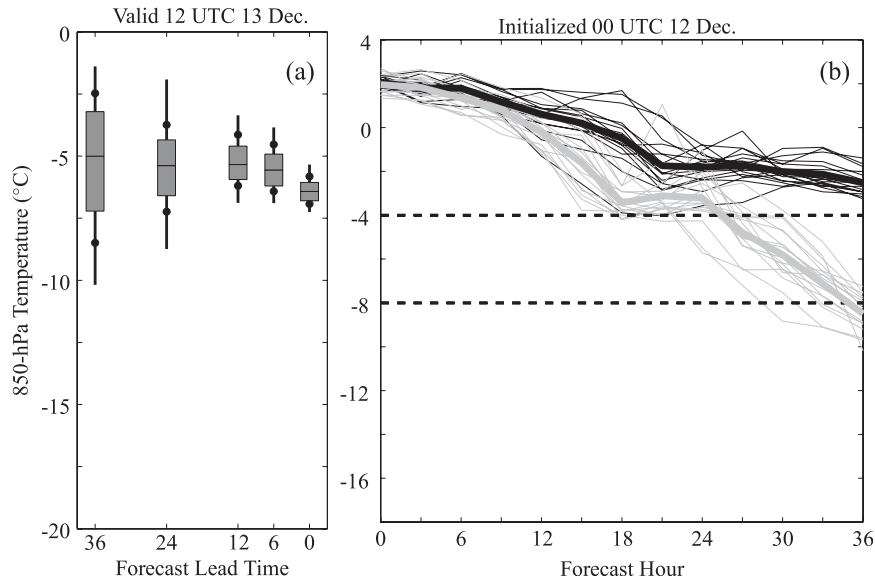


FIG. 4. (a) Box-and-whisker plots of the predicted 850-hPa temperature in the Puget Sound metric box at different lead times for forecasts valid at 1200 UTC 13 Dec 2008. (b) The evolution of the 17 warmest (black) and coldest (gray) members for ensemble simulations initialized at 0000 UTC 12 Dec 2008. The solid thick lines show the 17-member subset means. The horizontal dashed lines indicate the temperatures at which precipitation is expected to fall as rain (above -4°C) or snow (below -8°C) in the Puget Sound region.

forecast hour for each member of the warm and cold subsets in Fig. 4b. Also shown by the thick lines are the behaviors of the warm- and cold-subset means. (No curves are shown for the 66 forecasts that fall within one σ of the ensemble mean.) The forecast temperatures remain relatively similar until forecast hour 24, after which they begin to diverge rapidly.

The evolution of the synoptic-scale features in the warm- and cold-subset means is compared in Fig. 5. Initial conditions for the warm- and cold-subset means are plotted in Figs. 5a,b for 0000 UTC 12 December 2008, which is the analysis time for the 36-h forecasts. The upper-level potential vorticity (PV) distribution [shown by the shaded contours of θ on the 2-potential vorticity unit (PVU) surface], the lower-level thermal field (shown by the white contour lines of 850-hPa temperature), and the surface pressure fields for both subset means appear very similar at the initial time. Twelve hours later a short wave is apparent to the west of Vancouver Island in the warm-subset mean (Fig. 5d); this feature is much weaker in the cold-subset mean (Fig. 5c). The differences apparent at 12 h continue to amplify, so that by forecast hour 36 the warm-subset mean shows a strong surface low just to the east of Puget Sound with a secondary low on the Montana–Idaho border (Fig. 5e), whereas the primary surface low in the cold subset is even farther east on the Montana–Wyoming border (Fig. 5f).

The large differences in the 36-h forecasts for the warm and cold subsets are not easy to anticipate on the basis of the very similar conditions used to initialize the members of both subsets. Twelve hours later, the differences between the two subsets are far more apparent: as shown in Fig. 6, the ensemble mean for the EnKF assimilation of the 1200 UTC 12 December 2008 observations clearly captures the shortwave west of Vancouver Island. One might therefore expect that the warm-subset members will verify better than those in the cold subset. In fact, the verifying analysis at 1200 UTC 13 December gives a metric-box-averaged 850-hPa temperature of about -6.5°C , which does not lie in the 36-h forecast temperature range of either the warm or the cold subset, but rather is within one standard deviation of the ensemble mean (Fig. 4a). The verifying temperature of -6.5°C is actually closer to the temperatures in the cold subset than those in warm subset; it is also very close to the rain–snow borderline in the FMLP climatology. During the actual event, rain was reported at most surface stations in the metric box during the period 0600–1200 UTC 13 December (corresponding to forecast hours 30–36).

b. The 17–18 December case

The spread of the 850-hPa temperature metric for the second case, verifying at 1200 UTC 18 December, is shown as a function of forecast lead time by the box-and-whisker

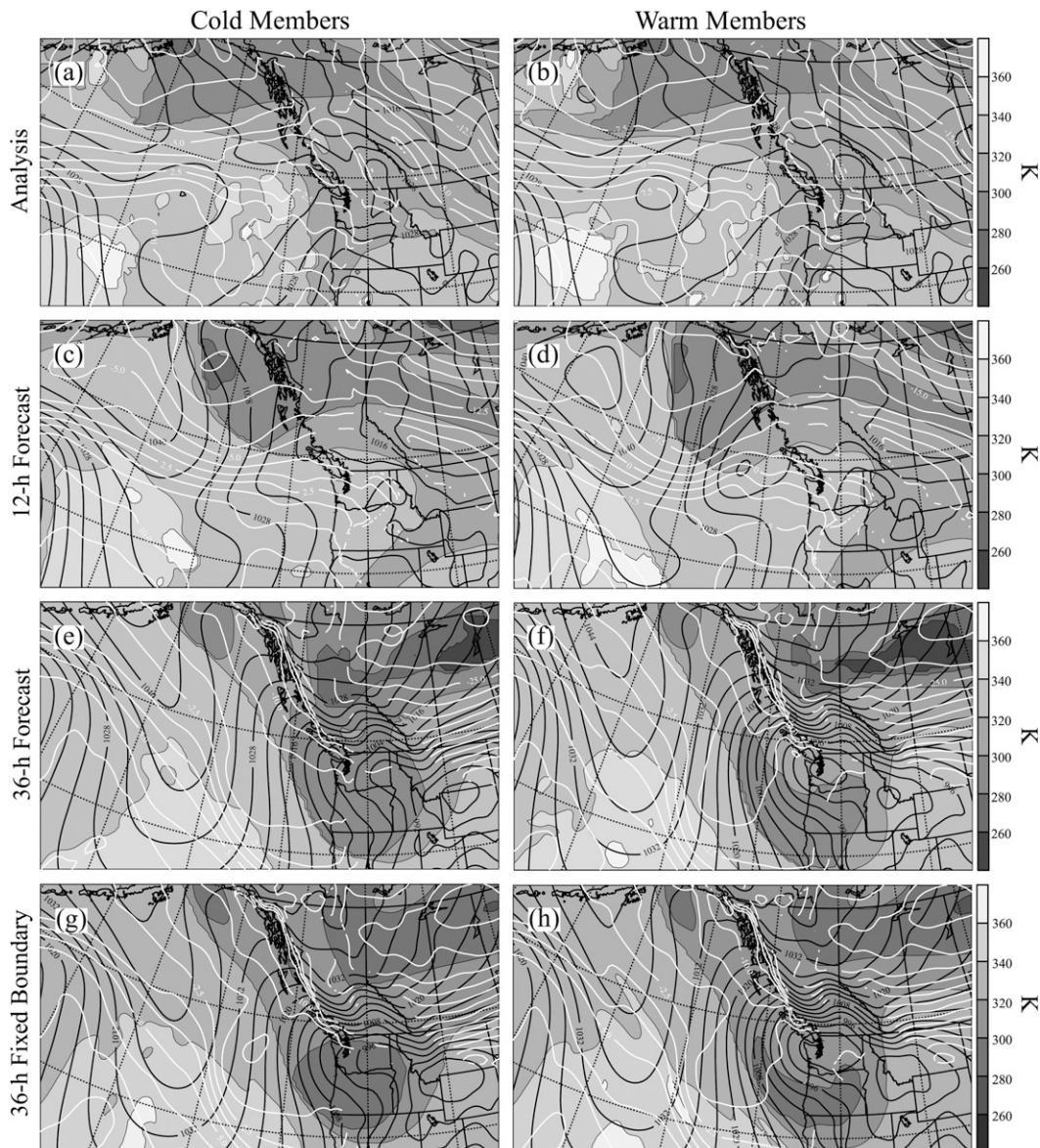


FIG. 5. The (a),(b) analysis, as well as the (c),(d) 12- and (e),(f) 36-h forecasts initialized for 0000 UTC 12 Dec 2008 on the 36-km domains for the (a),(c),(e) cold subset and (b),(d),(f) warm subset. (g),(h) As in (e),(f), except that all ensemble members used the same boundary conditions. Each panel shows θ on the 2-PVU surface (shaded), mean sea level pressure (MSLP; black contours), and 850-hPa temperature (white contours). Temperature contours are not plotted where the 850-hPa surface intersects the topography. The region shown is a subset of the full domain.

plot in Fig. 7a. By 36 h, the difference between warm- and cold-subset means increases to 9°C , which is much larger than the difference at the same lead time in the first case. This temperature difference accumulates at an almost constant rate between forecast hours 12 and 36. The 36-h temperatures themselves are relatively cold (warm- and cold-subset means of -6° and -15°C , respectively), so according to the FMLP climatology, any precipitation produced by the majority of the ensemble members would likely fall as snow. As will be discussed

in the next section, which examines the precipitation forecasts, the warm-subset events are accompanied by precipitation, but the cold-subset members are not, so in this case there is significant forecast uncertainty for both precipitation and temperature.

The evolution of the synoptic-scale features in this second case is shown by the warm- and cold-subset means plotted in Fig. 8. As in the previous case, the initial analyses for the two subset means are very similar (Figs. 8a,b). The differences between the two subsets that develop

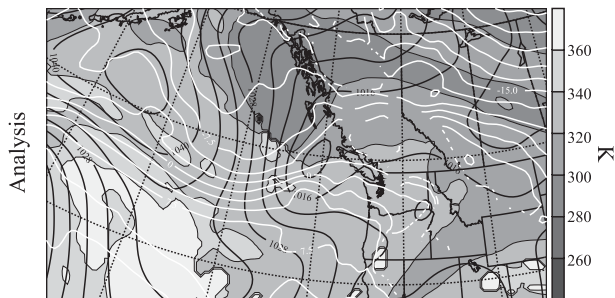


FIG. 6. The ensemble-mean analysis of θ on the 2-PVU surface (shaded), MSLP (black contours), and 850-hPa temperature (white contours) at 1200 UTC 12 Dec 2008.

12 h into the forecast are perhaps most pronounced in the structure of the trough just inland of the Canadian coast, which is somewhat stronger in the cold-subset mean (Figs. 8c,d). By forecast hour 36, the differences have become quite substantial: the trough is much deeper in the cold-subset mean and the surface low is centered over the Idaho panhandle, whereas in the warm-subset mean, the low center is just west of Puget Sound.

c. Behavior in the limit of identical lateral boundary data

As discussed in the introduction, overoptimistic estimates of mesoscale predictability have been obtained in identical-twin numerical experiments in which the same boundary conditions were imposed on each twin. The boundary conditions for our ensemble members are perturbed following the methodology in Torn et al. (2006), and one might wonder to what extent our ensemble spread is driven by the perturbations at our

boundaries. To assess this, the previous ensemble simulations were repeated with identical large-scale boundary conditions imposed on all the ensemble members. The evolution of the warm- and cold-subset 850-hPa metric-box temperatures in these identical-boundary ensembles follow the curves plotted in Fig. 9a,b, which should be compared with Figs. 4b and 7b, respectively. Most of the differences between the identical- and perturbed-boundary simulations appear after 24 h, and not surprisingly, the differences between the cold- and warm-subset temperatures are reduced when the ensemble members all use identical lateral boundary conditions. In the case beginning at 0000 UTC 12 December, the 36-h temperature spread between the cold- and warm-subset means is reduced from 5.5° to 4°C; in the case beginning 0000 UTC 17 December, it is reduced from 9° to 5.5°C. Previous investigations of mesoscale predictability have established that using identical lateral boundary conditions tends to overestimate the degree of predictability (Errico and Baumhefner 1987; Vukicevic and Paegle 1989; Vukicevic and Errico 1990), yet even with identical boundary conditions, the range of temperatures in our metric box is still large enough to introduce significant uncertainty into the rain–snow forecast.

The impact of using identical boundary data on the structure of synoptic-scale features in the 36-h ensemble forecasts may also be appreciated by examining Figs. 5 and 8. In the first 12–13 December case, comparing Figs. 5e,f with Figs. 5g,h shows the difference in the surface pressure field over the Pacific Northwest between the means of the warm and cold subsets is only slightly influenced by the presence or lack of ensemble perturbations at the lateral boundaries. The boundary

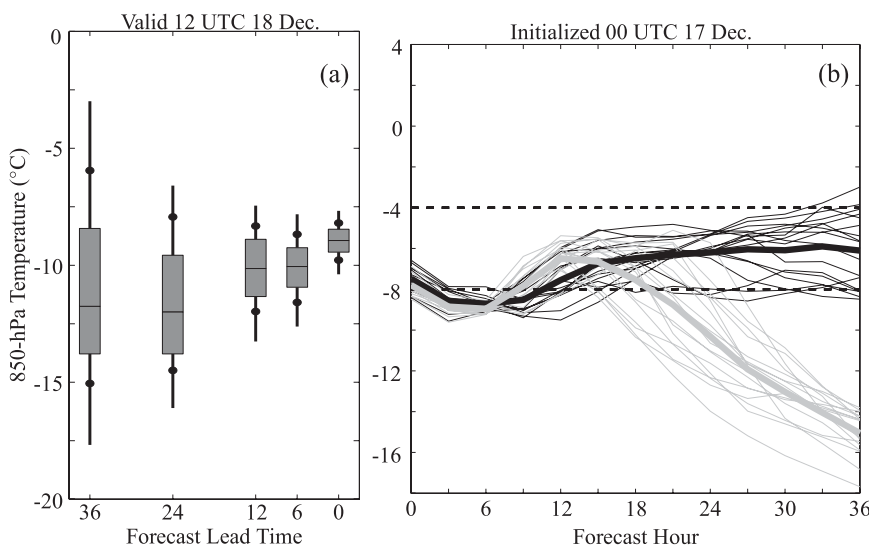


FIG. 7. As in Fig. 4, but for (a) forecasts valid at 1200 UTC 18 Dec 2008 and (b) an ensemble forecast initialized 0000 UTC 17 Dec 2008.

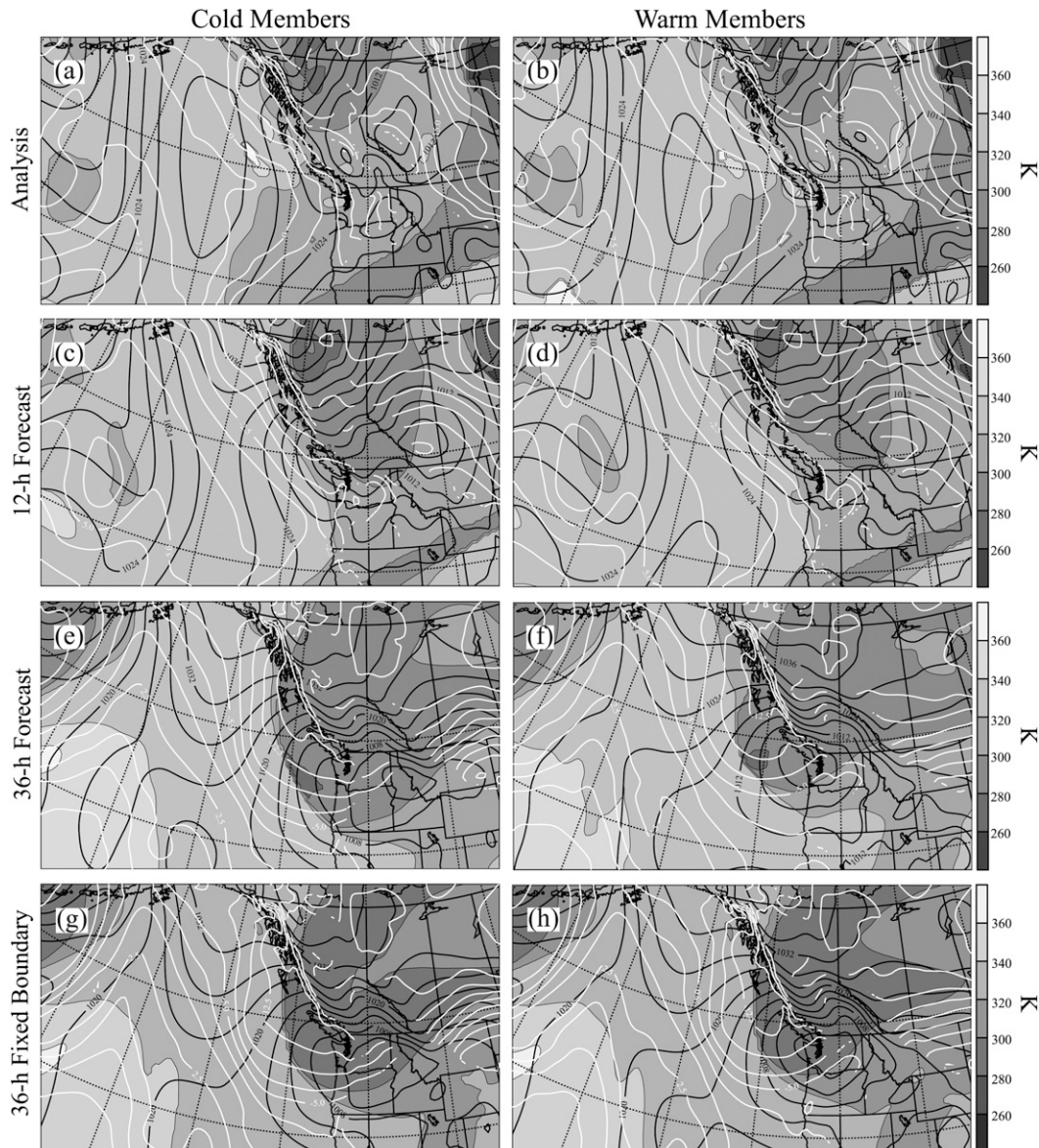


FIG. 8. As in Fig. 5, but for the forecast initialized at 0000 UTC 17 Dec 2008.

treatment has a greater impact on the upper-level PV structure, but similar qualitative differences between the warm- and cold-subset means are still preserved after the switch from perturbed to identical boundary data. Similar sensitivity is revealed for the second, 17–18 December, case in Figs. 8e–h.

4. Ensemble distribution of the accumulated precipitation

Of course snow requires the combination of precipitation and sufficiently cold temperatures, and in this section we compare the precipitation that develops in the

ensemble forecasts for these two events. The 18-h accumulated precipitation forecast for western Washington ending at 1200 UTC 13 December 2008 is plotted for the warm- and cold-subset means in Figs. 10a,b. These data are from the 36-h forecast initialized at 0000 UTC 12 December. Clearly more total precipitation is forecast for the metric box by the cold-subset members, while the coastal mountains of northern Oregon receive more precipitation in the warm-subset forecasts.

The relation between the precipitation and the 850-hPa temperature metric during the 12–13 December event is shown for the warm-subset, cold-subset, and full ensemble means in Fig. 11. Each panel in this figure

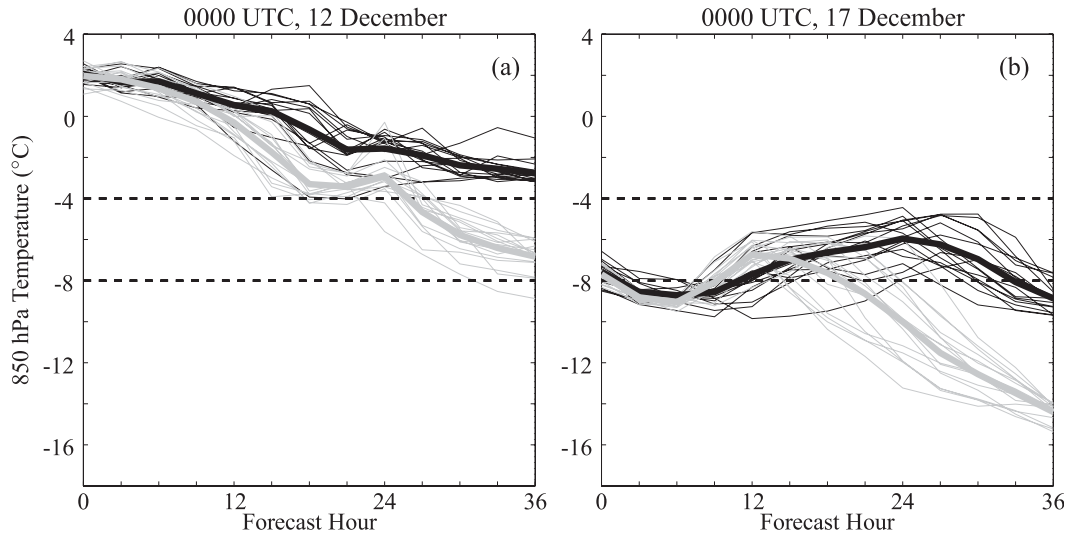


FIG. 9. As in (a) Fig. 4b and (b) Fig. 7b, but for ensembles with identical lateral boundary data.

shows 6-h precipitation totals binned by the 850-hPa temperature at each grid point within the metric box on the 12-km mesh. The temperature used to bin the precipitation at each point is the average of the temperatures at the beginning and the end of the 6-h interval over which the precipitation is accumulated.² Separate curves are plotted for the full 100-member ensemble, for the warm-subset members, and for those in the cold subset. The bin widths are 0.5°C, and the precipitation values are scaled such that the sum of the precipitation over all bins gives the 6-h precipitation averaged over the full metric box.

During the period between forecast hours 18 and 24, most of the precipitation in the full ensemble falls at 850-hPa temperatures warmer than -4°C , and according to the FMLP climatology, would likely be rain (Fig. 11a). Total precipitation is heaviest in the cold subset; it is lightest in the warm subset, and the precipitation amounts for the full ensemble lie in between. The range of temperatures at which precipitation falls in the warm subset is tighter than in either the cold subset or the full ensemble, and the narrow spread in 850-hPa temperature at which precipitation occurs in the warm subset becomes more pronounced during the last two forecast periods. In the 30–36-h forecast period virtually all the warm-subset precipitation inside the metric box is falling at 850-hPa temperatures between -4° and -1.5°C , and has a precipitation-weighted mean of -2.8°C . On the other hand, in the cold subset, some precipitation occurs

within the box at temperatures ranging from -10° to -4°C , with the precipitation-weighted mean occurring at -7.1°C . The FMLP climatology therefore suggests the 1σ warmest ensemble members are likely to produce rain over the period covered by forecast hours 30–36, whereas roughly half of the precipitation produced by the 1σ coldest members would likely be snow. The remaining precipitation from the cold-subset members, as well as roughly two-thirds of the precipitation in the total ensemble, falls in the temperature range between -8° and -4°C , within which the FMLP climatology gives less guidance about precipitation type.

The contrast between the warm- and cold-subset precipitation in the second case (17–18 December) is somewhat different. The horizontal distribution of the warm- and cold-subset-mean 18-h accumulated precipitation from 36-h forecasts initialized at 0000 UTC 17 December is compared in Figs. 10c,d. The cold-subset members produce little precipitation in the metric box during this period; most of their precipitation falls farther south in the Cascade Mountains of Oregon. The warm-subset members do, however, produce significant precipitation in the metric box and at other locations throughout western Washington.

The relation between the 850-hPa temperatures and the precipitation within the metric box in the 17–18 December event is shown in Fig. 12. During the first period (18–24 h), significant precipitation occurs in both the full ensemble and the warm and cold subsets; however, the precipitation in the warm subset is much heavier during the two later periods than that in the ensemble mean or the cold subset. The precipitation-weighted mean temperatures for the warm subset are relatively cold: -6.3°C over 18–24 h, -5.6°C over 24–30 h, and

² In both the 12–13 and 17–18 December events, the cold-subset temperatures at the end of the 36-h forecast (Figs. 4 and 7) are at least 1°C colder than the 30–36-h average temperature.

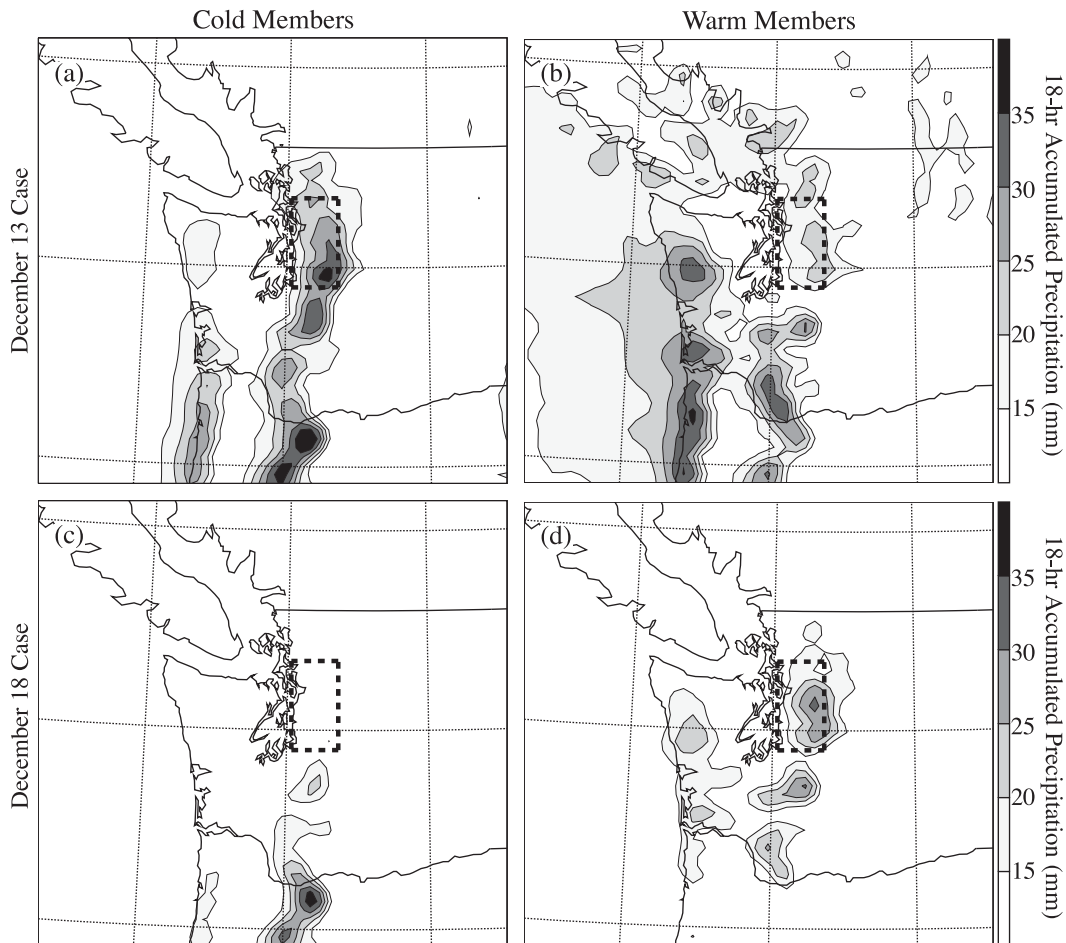


FIG. 10. The 18-h accumulated precipitation on the 12-km domain for the (a) cold- and (b) warm-subset means from the 36-h forecast ending 1200 UTC 13 Dec 2008 and for the (c) cold- and (d) warm-subset means from the 36-h forecast ending 1200 UTC 18 Dec 2008. The metric box is indicated by the thick dashed lines.

-5.0°C over 30–36 h. In contrast, there is very little precipitation during the last two periods in the cold subset, and that precipitation falls at very cold precipitation-weighted means of -10.1°C at 24–30 h and -13.0°C at 30–36 h. According to the FMLP climatology, most of the ensemble members in this event give a significant chance of snow, but there is considerable uncertainty about the amount of precipitation that will fall in the metric box over forecast hours 24–36. Snow was in fact reported at most surface stations within the metric box during the period 0600–1200 UTC 18 December (corresponding to forecast hours 30–36).

5. Scale interactions

Is the 36-h ensemble spread in these events produced by the upscale growth of initially small-scale perturbations? We explore this question by examining

the scale interactions responsible for the growth of the perturbations about the ensemble mean, focusing on the kinetic energy spectrum of these perturbations. All spectra are computed using data from the 12-km domain following a procedure similar to that in Skamarock (2004), which may be outlined as follows.

a. Evaluating the spectrum of perturbation kinetic energy

Let $u_{i,j,n}$ and $v_{i,j,n}$ respectively denote the zonal and meridional velocity components at 700 hPa³ for the n th ensemble member at zonal grid point i and meridional point j . The least squares-fit linear trends in $u_{i,j,n}$ and $v_{i,j,n}$ were removed along the zonal (i th) direction, then strict

³ 700 hPa is selected as the closest standard level to the 850-hPa metric box that generally lies above the terrain.

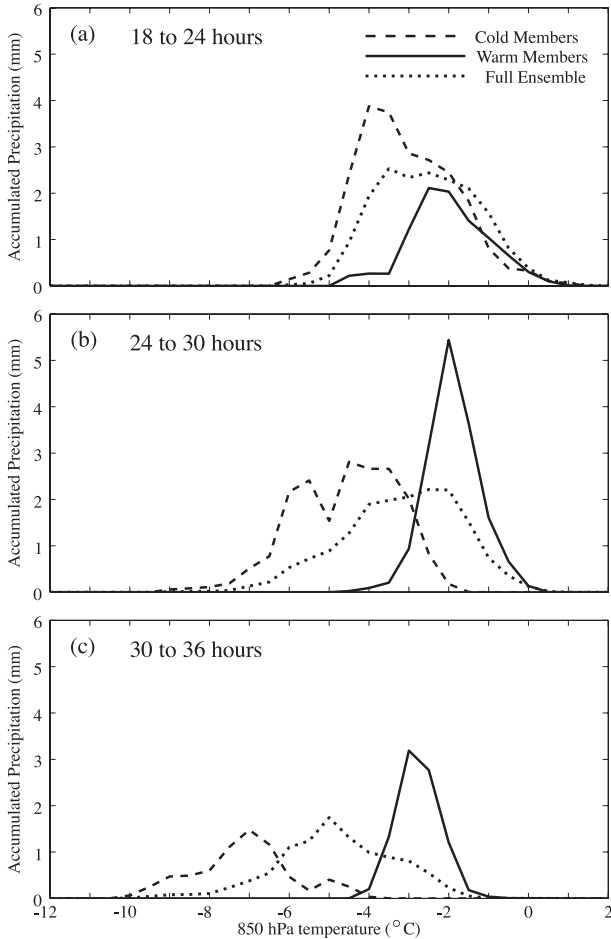


FIG. 11. Precipitation within the metric box as a function of 850-hPa temperature for the 12–13 December case. Precipitation for the warm-subset, cold-subset, and ensemble means is accumulated using the 12-km-domain data over the 6-h intervals from forecast hours (a) 18–24, (b) 24–30, and (c) 30–36.

periodicity was ensured by applying a cosine taper to the five grid points adjacent to the nested-grid boundary. Defining wavenumbers $k = 2\pi/\lambda$, where λ is the zonal wavelength, the Fourier transforms of the velocity components $\hat{u}_{j,n}(k)$ and $\hat{v}_{j,n}(k)$ were computed along the i th coordinate for each ensemble member and all j indices. Letting the asterisk denote the complex conjugate, one-dimensional kinetic energy density spectra were computed according to the formula

$$\widehat{\text{KE}}_{j,n}(k) = \frac{\Delta x}{2N_x} [\hat{u}_{j,n}(k)\hat{u}_{j,n}^*(k) + \hat{v}_{j,n}(k)\hat{v}_{j,n}^*(k)],$$

where N_x is the number of grid points along the i th coordinate and the leading factor ensures the discrete Parseval's theorem relating the x -integrated kinetic

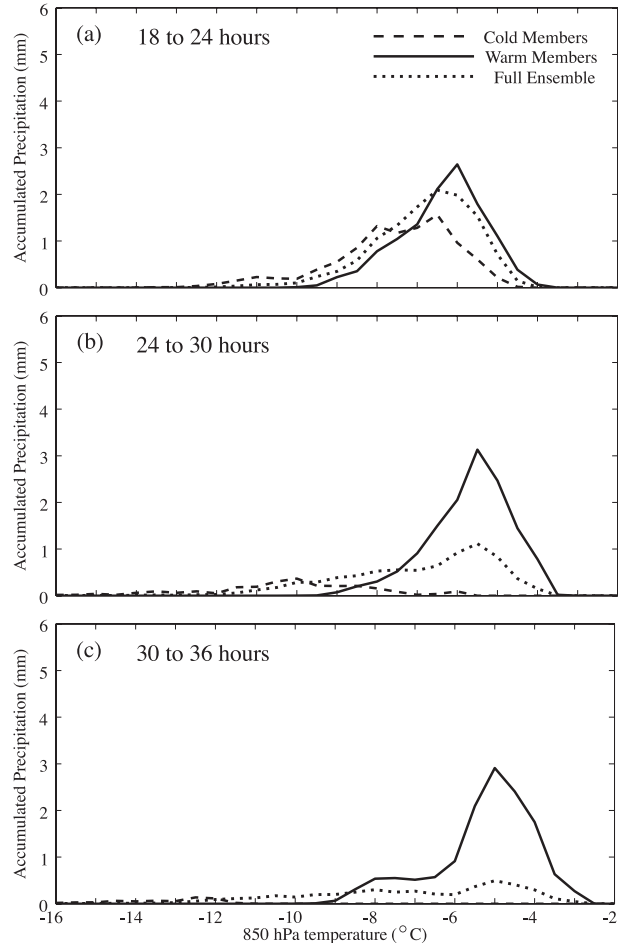


FIG. 12. As in Fig. 11, but for the 17–18 December case.

energy to the k -integrated energy density has the correct dimensional form. Then $\widehat{\text{KE}}_{j,n}(k)$ is averaged over all j and n to obtain $\widehat{\text{KE}}(k)$, the kinetic energy spectrum for the full ensemble.⁴ The spectrum of the kinetic energy of the perturbations about the ensemble mean, $\text{KE}'(k)$, was computed in a similar manner such that

$$\widehat{\text{KE}}'_{j,n}(k) = \frac{\Delta x}{2N_x} [\hat{u}'_{j,n}(k)\hat{u}'_{j,n}{}^*(k) + \hat{v}'_{j,n}(k)\hat{v}'_{j,n}{}^*(k)].$$

Figure 13 shows the spectrum of $\widehat{\text{KE}}$ at 700 hPa as a function of horizontal wavenumber k at the 12-h forecast time averaged between both events (i.e., between the forecasts for 1200 UTC 12 December and 17 December). Using the 12-h forecast instead of the initial analysis provides a better indication of the impact

⁴ Sensitivity tests in which the velocity components are first Fourier transformed in the j direction and then averaged in the i direction produce similar results.

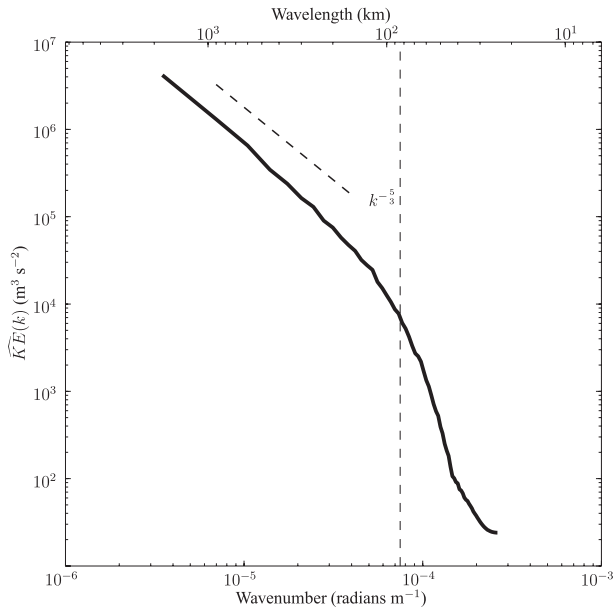


FIG. 13. (a) Average of the 700-hPa horizontal kinetic energy spectra over the two times: 1200 UTC 12 Dec and 1200 UTC 17 Dec 2008. Line with $k^{-5/3}$ slope is plotted for reference. The vertical dashed line represents the $7\Delta x$ wavelength.

of the model dynamics on the \widehat{KE} spectrum. Although Fig. 13 only shows ensemble data for two events, the \widehat{KE} spectrum is still similar to that obtained from averages over much longer periods using observations (Nastrom and Gage 1985) or mesoscale models (Skamarock 2004). In particular, the spectrum follows a slope of approximately $k^{-5/3}$ as the wavelength decreases to almost $7\Delta x$, after which point \widehat{KE} decreases more rapidly owing to numerical dissipation and horizontal smoothing.

b. The spectrum of \widehat{KE}' at the initial time

The spectra of the initial perturbations about the ensemble mean are plotted for both events (0000 UTC 12 December and 0000 UTC 17 December) as solid black lines in Figs. 14a,b. The power in \widehat{KE}' increases strongly with horizontal scale all the way up to the longest resolvable wavelength of almost 2000 km. This monotonic increase in \widehat{KE}' with wavelength is similar to that in the imperfect-twin mesoscale predictability experiments of Zhang et al. (2002) and Bei and Zhang (2007). In both of these previous studies, the initial differences between the twins arise because of the use of different data assimilation schemes (i.e., to differences in physical space), and the energy spectrum of those initial differences is maximized at the longest resolved wavelengths.

In contrast, those investigations of mesoscale predictability that begin with idealized perturbations added to control simulations often specify initial perturbation

spectra that are either flat (white noise⁵) or maximized at short wavelengths (Tan et al. 2004; Zhang et al. 2007). Maximizing the initial perturbation energy at the shortest wavelengths facilitates comparisons with the upscale energy cascade predicted by classical spectral models of turbulence (Lorenz 1969; Rotunno and Snyder 2008) but may not approximate the typical structure of initial-condition uncertainties in the atmosphere.

One complication with spectral descriptions of atmospheric perturbations is that the individual modes are not local, but rather extend with uniform amplitude throughout the entire domain. Thus, the spatial structure of a spectral perturbation in which energy appears only at the shortest resolved scale consists of a repeated series of essentially identical small-scale fluctuations. On the other hand, a small-scale disturbance that is localized in space has an energy spectrum with maximum power at the longest wavelengths. As a simple example, consider a one-dimensional field with a perturbation of small characteristic spatial scale a , and suppose the difference between one ensemble member and the ensemble mean consists of a linear barotropic shear flow

$$v_1'(x, y, z) = v_0 e^{-x^2/a^2}.$$

The dependence of the perturbations on the x -coordinate wavenumber k , obtained by Fourier transforming with respect to x , is

$$\widehat{v}_1'(k) = \int_{-\infty}^{\infty} v_1'(x) e^{-ikx} dx = v_0 \sqrt{\pi} a e^{-a^2 k^2/4}. \quad (1)$$

Denoting the complex conjugate by an overbar, the power spectrum of v_1' ,

$$\frac{\widehat{v}_1' \widehat{v}_1'^*}{2} = \frac{v_0^2}{2} \pi a^2 e^{-a^2 k^2/2}, \quad (2)$$

is clearly maximized at the longest wavelengths (i.e., the smallest wavenumbers). A real-world example of this type is provided by the spectrum of the “disturbance kinetic energy” in an experiment in which a single sounding was omitted from the data assimilation step for a “disturbed” simulation in Zhang et al. (2002). (See dotted curve labeled “NoLZK” in their Fig. 13a.)

If the functional form of v' is modified so that its mean is zero, the maximum of $\widehat{v}' \widehat{v}'^*$ no longer occurs at $k = 0$,

⁵ The one-dimensional spectrum (such as those plotted in this paper) of white noise is uniform in wavelength, whereas the two-dimensional spectrum of white noise is inversely proportional to the two-dimensional wavelength.

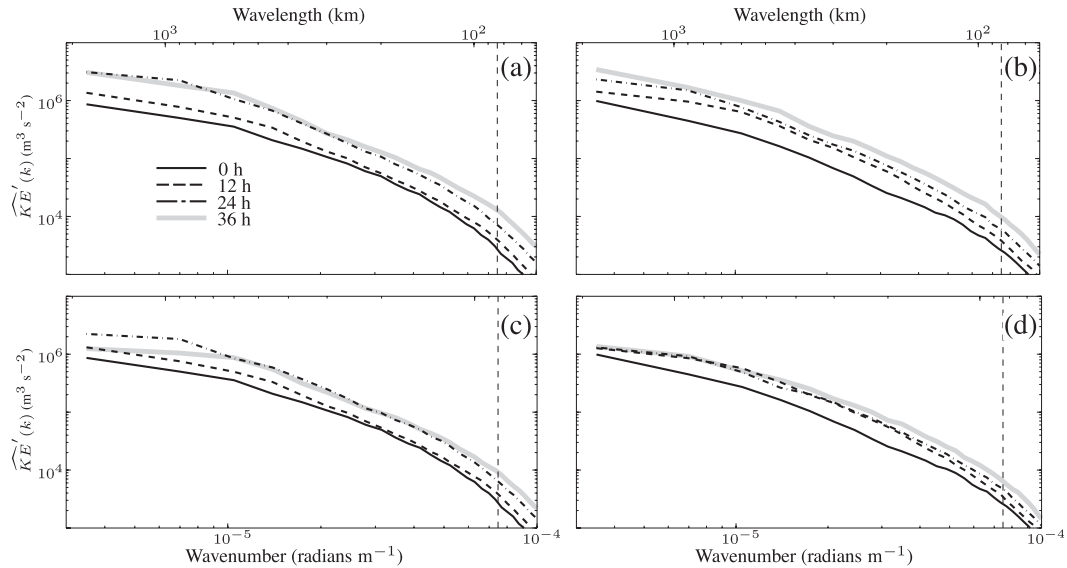


FIG. 14. The perturbation kinetic energy at 700 hPa as a function of forecast lead time for (a) the 0000 UTC 12 Dec forecast with perturbed lateral boundary values and (b) the 0000 UTC 17 Dec forecast with perturbed boundaries. (c),(d) As in (a) and (b), respectively, but for forecasts with unperturbed boundaries. The vertical dashed line represents the $7\Delta x$ wavelength. Wavenumbers less than 10^{-4} radians m^{-1} , which are subject to significant numerical damping, are omitted for clarity.

but it still may occur at a value of k that is largely independent of the scale of the local perturbation a . As a second example, suppose the perturbations in v' now consist of two Gaussians of opposite sign, separated by a distance L . Then letting

$$v'_2(x, y, z) = v_0 e^{-x^2/a^2} - v_0 e^{-(x-L)^2/a^2},$$

one obtains

$$\widehat{v}'_2(k) = v_0 \sqrt{\pi} a e^{-a^2 k^2/4} (1 - e^{ikL})$$

and

$$\frac{\widehat{v}'_2 \widehat{v}'_2^*}{2} = v_0^2 \pi a^2 e^{-a^2 k^2/2} [1 - \cos(kL)]. \quad (3)$$

According to (3), the spectral power in $\widehat{v}'_2 \widehat{v}'_2^*$ drops to zero at wavenumbers $k = 2n\pi/L$, $n = 0, 1, 2, \dots$. The maxima in $\widehat{v}'_2 \widehat{v}'_2^*$ occur between these zeros, and if $L \gg a$, the global maximum is near π/L . Thus, the maximum in the spectral power of v'_2 is set by the distance between the perturbations (e.g., a pair of thunderstorms), not by the scale of the perturbations themselves.⁶

⁶ If $L \approx a$, the global maximum of $\widehat{v}'_2 \widehat{v}'_2^*$ still occurs at some point in the interval $0 \leq k \leq 2\pi/L$, but the location of that point depends more strongly on the value of a .

While isolated small-scale differences will tend to produce an initial spectrum of \widehat{KE}' with maximum power in the longest wavelengths, it is not certain whether the amplitude of such accumulated differences would be sufficient to produce the actual initial values of \widehat{KE}' seen at the large scales in Figs. 14a,b. Slight shifts in the position of the phase of the long waves might alternatively be responsible. Suppose a now represents the small distance by which a large-scale wave is shifted relative to the phase of the ensemble mean. Then the velocity perturbation takes the form

$$v'_3(x, y, z) = u_0 \cos[k(x - a)] - u_0 \cos(kx).$$

If the shift is small compared to the wavelength, $ka \ll 1$ and expanding $\cos(kx)$ and $\sin(kx)$ in Taylor series gives

$$v'_3(x, y, z) \approx u_0 ka \sin(kx).$$

The coefficient of the Fourier series at wavenumber k is therefore $u_0 ka$, and the spectral power at wavenumber k is

$$\frac{\widehat{v}'_3 \widehat{v}'_3^*}{2} = \frac{u_0^2 k^2 a^2}{2}. \quad (4)$$

To compare the power at wavenumber k for the shifted wave to that for the isolated Gaussian (2), note that unlike the coefficients for Fourier series, the integral (1) defining

the Fourier transform is not normalized by the width of the domain (which, of course, is infinite). The coefficients of the Fourier series for an isolated Gaussian in a large domain of width $2D$, with $D \gg a$, will be approximately $\widehat{v}_1(k)/D$. The ratio of the spectral power at wavenumber k in the Gaussian to that in the shifted wave is, therefore, approximately

$$\frac{v_0^2 \pi e^{-a^2 k^2/2}}{u_0^2 k^2 D^2}.$$

For the longest waves in the domain, $\pi/(kD)^2$ is $O(1)$ and $ak \ll 1$, implying the ratio of the spectral power in a Gaussian perturbation of width a to that in a long wave shifted a small distance a is roughly equal to $(v_0/u_0)^2$, the square of the ratio of the maximum velocity in the Gaussian to the maximum velocity in the long wave. For small localized perturbations, such as those introduced by an extra radiosonde observation, this ratio could easily be less than 10^{-2} . On the other hand, if the Gaussian perturbation is supposed to represent an incorrectly placed thunderstorm, this ratio could approach unity.

c. Evolution of the spectrum of \widehat{KE}'

The growth in the spectrum of \widehat{KE}' over each 12-h period in the 36-h forecast may be determined from Fig. 14. In the first case (12–13 December, Fig. 14a), both short- and long-wavelength perturbations grow modestly over the first 12 h. Pronounced amplification subsequently occurs at all scales over the period 12–24 h. The variance of the perturbations appears saturated (no further growth occurs) at scales larger than about 200 km during the last period (24–36 h), but vigorous growth continues to occur at wavelengths in the range 40–80 km. In the second case (17–18 December, Fig. 14b), \widehat{KE}' grows significantly over the first 12 h at all scales longer than about 100 km. Over the next 12 h moderate growth occurs at those scales less than 200 km or greater than 700 km. Moderate growth continues at all scales over the final 12-h period, except there is some suggestion of saturation at wavelengths around 800 km.

The limits to predictability in a turbulent fluid with an energy spectrum shallower than k^{-3} are classically described as arising from errors in the smallest scales that perturb slightly larger-scale motions, which in turn introduce errors in yet larger scales, thereby leading to an upscale progression of uncertainty. This progression is illustrated for a system with a $k^{-5/3}$ spectrum in Fig. 1a of Rotunno and Snyder (2008), which shows the evolution of the error-energy spectrum in a case where all initial error was confined to the smallest retained scale. Their spectrum evolves in a fundamentally different manner from the \widehat{KE}' spectra shown in Figs. 14a,b, in which there

is significant initial error and simultaneous error growth at essentially all scales. The implications of this for mesoscale predictability will be discussed in the next section.

The self-similar shapes of the evolving \widehat{KE}' spectra in Figs. 14a,b seem to arise because the EnKF data assimilation does not significantly change the shape of the spectrum as it maps the ensemble spread generated by the previous 6-h forecast (the prior) into the initial ensemble used in the subsequent forecast (the posterior). A detailed investigation of the influence of the EnKF data assimilation cycle on the spectrum of \widehat{KE}' will be deferred to a subsequent paper.

Consistent with previous findings that imperfect-twin coarse-resolution mesoscale predictability experiments using identical lateral boundary conditions tend to generate pairs of forecasts with artificially reduced spread (Errico and Baumhefner 1987; Vukicevic and Paegle 1989; Vukicevic and Errico 1990), eliminating the ensemble variability at the lateral boundaries in these simulations greatly reduces the growth in \widehat{KE}' . This reduction in \widehat{KE}' is not limited just to those scales that are well resolved on the 36-km mesh (roughly wavelengths larger than 300 km) on which the lateral boundary conditions are applied, but is also apparent at all smaller scales. We hypothesize this reduction in small-scale \widehat{KE}' is produced by a reduction in the downscale growth of the ensemble perturbations owing to the decrease in large-scale \widehat{KE}' when identical lateral boundary conditions are imposed on all ensemble members on the 36-km domain. The possible importance of downscale error growth will be discussed further in the next section.

6. Discussion and conclusions

We have examined the spread among 100-member ensemble simulations for two cases where developing cyclones brought a threat of snow to the Puget Sound lowlands. In both cases, the ensemble spread grows with sufficient rapidity to introduce significant uncertainty in the rain–snow forecast at 36-h lead times. Our focus has not simply been on minor perturbations to the rain–snow boundary, which will always be a difficult forecast problem, but rather on situations where those ensemble members that are one standard deviation warmer and colder than the mean might be expected to have different outcomes (i.e., where there are significant numbers of both rain-likely and snow-likely outcomes). Model sensitivities to boundary layer and ice-microphysical parameterizations were avoided by focusing on the 850-hPa temperature during precipitation events using the climatology of FMLP, which suggests a transition between rain-likely and snow-likely events occurs as the 850-hPa

temperature decreases over an interval of 4°C (from -4° to -8°C in the Quillayute sounding).

In the first case (verifying at 1200 UTC 13 December 2008), the simulated 850-hPa-temperature difference between the means of the 17 warmest and the 17 coldest ensemble members grows to 5.5°C at 36 h (with metric-box averages of -2.5° and -8°C). Precipitation occurs in both subsets. Based on the FMLP climatology, at 36 h all the precipitation from the warm-subset members would likely fall as rain, while half of the precipitation from the cold-subset members would likely be snow. The second case (verifying at 1200 UTC 18 December 2008) is colder, with a wider 9°C spread at 36 h between the warm-subset and cold-subset means, which have metric-box averages of -6° and -15°C, respectively. Most of the precipitation during the 30–36-h forecast period occurs in the warm-subset members at temperatures straddling the rain–snow borderline, so the uncertainty in this case is more between a cold/dry event and a somewhat warmer rain/snow event.

The initial distribution of \widehat{KE}' , the perturbation kinetic energy of the ensemble members about the ensemble mean, increases monotonically with wavelength and is maximized at the longest wavelengths captured on our fine mesh (roughly 2000 km). This initial distribution appears to be produced by the tendency of our EnKF data assimilation cycle to roughly preserve the spectral shape of \widehat{KE}' when mapping the previous 6-h forecasts onto the new ensemble initial conditions—a behavior that is the subject of continuing investigation. Physically, the tendency of the initial \widehat{KE}' to be maximized at long wavelengths appears to be due to a combination of small phase shifts in the long waves and the presence of localized small-scale perturbations among the ensemble members. As illustrated by the theoretical examples in section 5, even if the differences between two fields are localized in small regions of physical space, the spectral energy density of their difference field is typically maximized at much larger scales.

In both events, the large-scale contributions to \widehat{KE}' (e.g., at wavelengths of 500 km) grow more rapidly over the first 12 h than those at the smallest resolved scales (i.e., at $7\Delta x = 84$ km; see Figs. 14a,b). There is no indication that small-scale disturbances develop more rapidly and then modify the larger scales. Rapid perturbation growth in the large scales, without prior upscale triggering, was also noted by Tribbia and Baumhefner (2004), who found synoptic-scale disturbance growth to be insensitive to the presence of perturbations at wavelengths shorter than spherical wavenumber 30.

Large-scale variations quickly perturb the smaller scales. The rapidity with which perturbations in the large scales amplify those in the small scales was recognized in

the seminal work by Lorenz (1969) and recently re-emphasized in Rotunno and Snyder (2008). These authors computed scale-dependent interaction coefficients for idealized turbulence models, showing that for systems in which the spectral energy density is proportional to $k^{-5/3}$, perturbations spread most rapidly from the large scales to the small scales. The primary focus of Lorenz (1969) was on determining whether fluid systems possess an “intrinsic finite range of predictability” that cannot be lengthened by reducing the observational errors at arbitrarily small scales to any value greater than zero. Nevertheless, Lorenz’s analysis of the same idealized fluid system also implies that errors at the smallest scales can be generated most efficiently by placing perturbations of a given absolute magnitude at the largest possible scale. This is evident both from the interaction coefficients in his Table 2 and by comparing his numerical experiments A and B. Lorenz placed initial errors of identical magnitude at the smallest scale in experiment A and at the largest scale in B. Since the background energy in Lorenz’s model was 10^3 greater at the largest scale than at the smallest scale, the relative error in the largest scale in experiment B was 10^{-3} less than the relative error placed at the smallest scale in experiment A. Yet predictability at the smallest resolved scales was lost almost twice as fast owing to downscale error propagation in experiment B than because of the growth of errors originating at the small scales in experiment A (see the first line of his Table 3). In addition to informing us about the intrinsic predictability of certain fluid systems, Lorenz’s results also suggest that there may be practical limits on the predictability of small-scale motions in systems with spectral energy density proportional to $k^{-5/3}$, because it may not be feasible to keep the relative errors in the large-scale initial conditions sufficiently small.

At scales larger than about 500 km, the atmospheric kinetic energy spectrum is proportional to k^{-3} (Nastrom and Gage 1985), and as noted by Rotunno and Snyder (2008), errors propagate much more slowly downscale in such systems than in those with a $k^{-5/3}$ energy spectrum (cf. the entries in the lower-left corners of Rotunno and Snyder’s Tables 3 and 4). Since the slope of the atmospheric kinetic energy spectrum flattens to $k^{-5/3}$ for wavelengths shorter than 500 km, downscale error growth is likely to be more of a problem for mesoscale predictability than for the predictability of the synoptic-scale flow.

Many recent studies of mesoscale predictability focus on the very real challenges presented by the upscale influence of small-scale phenomena like energetic deep convection (Hohenegger and Schär 2007; Zhang et al. 2007). For example, Zhang et al. (2003) examined the

predictability of the 24–25 January 2000 East Coast snowstorm and found that the “growth of initial errors from convective scales places an intrinsic limit on the predictability of larger scales” over forecast periods of 1–2 days. In contrast, Langland et al. (2002) explored the predictability of this same snowstorm over slightly longer 3-day forecasts and found the synoptic-scale evolution of the cyclone to be very sensitive to small-amplitude large-scale perturbations in the upstream flow.

We are only aware of a few previous papers suggesting that the predictability of mesoscale circulations may be limited by very small errors in the larger scales. Results consistent with this hypothesis were, nevertheless, obtained by Nuss and Miller (2001), who noted that slight rotations of the topography relative to the oncoming synoptic-scale flow can have a dramatic influence on terrain-induced mesoscale circulations, by Bei and Zhang (2007), who found that large-scale differences in imperfect-twin simulations of a mei-yu-front heavy-precipitation event can rapidly generate significant perturbations in the precipitation field, and by Reinecke and Durran (2009a), who found that the spread of ensemble forecasts of downslope winds can be extremely sensitive to small variations in the larger-scale flow at lead times ranging from 6 to 12 h.

The differences in the initial conditions for the warm and cold-subset means in our simulations (cf. Figures 5a,b and Figs. 8a,b) appear to be quite small, but they grow to become significant in just 36 h. Our cases involve amplifying short-wave troughs, and it seems likely that the sensitivities to initial conditions are weaker in more quiescent dynamical regimes. Further research is needed to better characterize the sensitivity of various types of mesoscale circulations to small errors in the synoptic-scale analysis.

Acknowledgments. The authors are grateful to Rich Rotunno, Chris Bretherton, Carolyn Reynolds, Tony Eckel, and Mark Gingrich for illuminating conversations, and for comments from an anonymous reviewer. D.R.D.’s research was supported by the Office of Naval Research Grant N00014-11-1-0331 and NSF Grant ATM-083616. The second and third authors acknowledge the support of the Chief of Naval Research through Program Element 0601153N of the NRL Base Program.

REFERENCES

- Anthes, R. A., Y. Kuo, D. P. Baumhelfner, R. M. Errico, and T. W. Bettge, 1985: Prediction of mesoscale atmospheric motions. *Advances in Geophysics*, Vol. 28B, Academic Press, 159–202.
- Barker, D. M., W. Huang, Y. R. Guo, A. J. Bourgeois, and Q. N. Xiao, 2004: A three-dimensional variational data assimilation system for MM5: Implementation and initial results. *Mon. Wea. Rev.*, **132**, 897–214.
- Bei, N., and F. Zhang, 2007: Impacts of initial condition errors on mesoscale predictability of heavy precipitation along the Mei-Yu front of China. *Quart. J. Roy. Meteor. Soc.*, **133**, 83–99.
- Doyle, J. D., V. Grubišić, O. J. Brown, S. F. J. De Wekker, A. Dörnbrack, Q. Jiang, S. D. Mayor, and M. Weissmann, 2009: Observations and numerical simulations of subrotor vortices during T-REX. *J. Atmos. Sci.*, **66**, 1229–1249.
- , Q. Jiang, and V. Grubišić, 2011: Three-dimensional characteristics of stratospheric mountain waves during T-REX. *Mon. Wea. Rev.*, **139**, 3–23.
- Errico, R. M., and D. Baumhelfner, 1987: Predictability experiments using a high-resolution limited-area model. *Mon. Wea. Rev.*, **115**, 488–504.
- Ferber, G. K., C. F. Mass, G. M. Lackmann, and M. W. Patnoe, 1993: Snowstorms over the Puget Sound lowlands. *Wea. Forecasting*, **8**, 481–504.
- Gaspari, G., and S. E. Cohn, 1999: Construction of correlation functions in two and three dimensions. *Quart. J. Roy. Meteor. Soc.*, **125**, 723–757.
- Harshvardhan, R. Davies, D. Randall, and T. Corsetti, 1987: A fast radiation parameterization for atmospheric circulation models. *J. Geophys. Res.*, **92** (D1), 1009–1015.
- Hodur, R. M., 1997: The Naval Research Laboratory’s Coupled Ocean/Atmosphere Mesoscale Prediction System (COAMPS). *Mon. Wea. Rev.*, **125**, 1414–1430.
- Hohenegger, C., and C. Schär, 2007: Atmospheric predictability at synoptic versus cloud-resolving scales. *Bull. Amer. Meteor. Soc.*, **88**, 1783–1793.
- Jiang, Q., and J. Doyle, 2009: The impact of moisture on mountain waves during T-REX. *Mon. Wea. Rev.*, **137**, 3888–3906.
- Kain, J. S., and J. M. Fritsch, 1993: Convective parameterization for mesoscale models: The Kain-Fritsch scheme. *The Representation of Cumulus Convection in Numerical Models*, Meteor. Monogr., No. 46, Amer. Meteor. Soc., 165–170.
- Klemp, J., and R. Wilhelmson, 1978: The simulation of three-dimensional convective storm dynamics. *J. Atmos. Sci.*, **35**, 1070–1096.
- Langland, R. H., M. A. Shapiro, and R. Gelaro, 2002: Initial condition sensitivity and error growth in forecasts of the 25 January 2000 East Coast snowstorm. *Mon. Wea. Rev.*, **130**, 957–974.
- Laprise, R., R. V. Mundakkara, B. Denis, and D. Caya, 2000: Predictability of a nested limited-area model. *Mon. Wea. Rev.*, **128**, 4149–4154.
- Lorenz, E. N., 1969: The predictability of a flow which possesses many scale of motion. *Tellus*, **21**, 289–307.
- Louis, J. F., 1979: A parametric model of vertical eddy fluxes in the atmosphere. *Bound.-Layer Meteor.*, **17**, 187–202.
- Mass, C. F., D. Ovens, K. Westrick, and B. A. Colle, 2002: Does increasing horizontal resolution produce more skillful forecasts? *Bull. Amer. Meteor. Soc.*, **83**, 407–430.
- Nastrom, G., and K. Gage, 1985: A climatology of atmospheric wavenumber spectra of wind and temperature observed by commercial aircraft. *J. Atmos. Sci.*, **42**, 950–960.
- Nuss, W. A., and D. K. Miller, 2001: Mesoscale predictability under various synoptic regimes. *Nonlinear Processes Geophys.*, **8**, 429–438.
- Reinecke, P. A., and D. R. Durran, 2009a: Initial-condition sensitivities and the predictability of downslope winds. *J. Atmos. Sci.*, **66**, 3401–3418.
- , and —, 2009b: The overamplification of gravity waves in numerical solutions to flow over topography. *Mon. Wea. Rev.*, **137**, 1533–1549.

- Rotunno, R., and C. Snyder, 2008: A generalization of Lorenz's model for the predictability of flows with many scales of motion. *J. Atmos. Sci.*, **65**, 1063–1076.
- Rutledge, S. A., and P. V. Hobbs, 1983: The mesoscale and microscale structure of organization of clouds and precipitation in midlatitude cyclones. VIII: A model for the “seeder-feeder” process in warm-frontal rainbands. *J. Atmos. Sci.*, **40**, 1185–1206.
- Skamarock, W. C., 2004: Evaluating mesoscale NWP models using kinetic energy spectra. *Mon. Wea. Rev.*, **132**, 3019–3024.
- Tan, Z.-M., F. Zhang, R. Rotunno, and C. Snyder, 2004: Mesoscale predictability of moist baroclinic waves: Experiments with parameterized convection. *J. Atmos. Sci.*, **61**, 1794–1804.
- Thériault, J. M., R. E. Stewart, and W. Henson, 2010: On the dependence of winter precipitation types on temperature, precipitation rate, and associated features. *J. Appl. Meteor. Climatol.*, **49**, 1429–1442.
- Torn, R. D., and G. J. Hakim, 2008: Performance characteristics of a pseudo-operational ensemble Kalman filter. *Mon. Wea. Rev.*, **136**, 3947–3963.
- , —, and C. Snyder, 2006: Boundary conditions for limited-area ensemble Kalman filters. *Mon. Wea. Rev.*, **134**, 2490–2502.
- Tribbia, J., and D. Baumhefner, 2004: Scale interactions and atmospheric predictability: An updated perspective. *Mon. Wea. Rev.*, **132**, 703–713.
- Vukicevic, T., and J. Paegle, 1989: The influence of one-way interacting boundary conditions upon predictability of flow in bounded numerical models. *Mon. Wea. Rev.*, **117**, 340–350.
- , and R. Errico, 1990: The influence of artificial and physical factors upon predictability estimates using a complex limited-area model. *Mon. Wea. Rev.*, **118**, 1460–1482.
- Whitaker, J. S., and T. M. Hamill, 2002: Ensemble data assimilation without perturbed observations. *Mon. Wea. Rev.*, **130**, 1913–1924.
- Zhang, F., C. Snyder, and R. Rottuno, 2002: Mesoscale predictability of the “surprise” snowstorm of 24–25 January 2000. *Mon. Wea. Rev.*, **130**, 1617–1632.
- , —, and —, 2003: Effects of moist convection on mesoscale predictability. *J. Atmos. Sci.*, **60**, 1173–1185.
- , —, and J. Sun, 2004: Impacts of initial estimate and observation availability on convective-scale data assimilation with an ensemble Kalman filter. *Mon. Wea. Rev.*, **132**, 1238–1253.
- , N. Bei, R. Rottuno, C. Snyder, and C. C. Epifanio, 2007: Mesoscale predictability of moist baroclinic waves: Convective-permitting experiments and multistage error growth dynamics. *J. Atmos. Sci.*, **64**, 3579–3594.